Analysis of the NGXO telescope x-ray Hartmann data

Timo T. Saha, Kai-Wing Chan, James R Mazzarella, Ryan S. McClelland, Peter M. Solly, et al.

Timo T. Saha, Kai-Wing Chan, James R Mazzarella, Ryan S. McClelland, Peter M. Solly, William W. Zhang, Vadim Burwitz, Gisela Hartner, Marlis-Madeleine La Caria, Carlo Pelliciari, "Analysis of the NGXO telescope x-ray Hartmann data," Proc. SPIE 10699, Space Telescopes and Instrumentation 2018: Ultraviolet to Gamma Ray, 1069952 (6 July 2018); doi: 10.1117/12.2312243

SPIE.

Event: SPIE Astronomical Telescopes + Instrumentation, 2018, Austin, Texas, United States

Analysis of the NGXO telescope X-ray Hartmann data

Timo T. Saha[a], Kai-Wing Chan[b], James R. Mazzarella[c], Ryan S. McClelland[a], Peter M. Solly[c], and William W. Zhang[a], Vadim Burwitz[d], Gisela Hartner[d], Marlis-Madeleine La Caria[d], and Carlo Pelliciari[d]

[a] NASA/Goddard Space Flight Center, Greenbelt, MD 20771

[b]Center for Research and Exploration in Space Science and Technology & University of Maryland, Baltimore County, Baltimore, MD 21250

[c] Stinger Ghaffarian Technologies, Inc., Greenbelt, MD 20770

[d]Max-Planck-Institute for extraterrestrial Physics, D-85748 Garching, Germany

ABSTRACT

Next Generation X-ray Optics (NGXO) team at the Goddard Space Flight Center (GSFC) has been developing a new silicon-based grazing incidence mirror technology for future high resolution X-ray astronomical missions. Recently, the GSFC team completed the construction of first few mirror modules that contain one pair of mirrors. One of the mirror pairs was tested in GSFC 600-m long beamline facility and PANTER (Neuried, Germany) 120-m long X-ray beamline facility. Both full aperture X-ray tests, Hartmann tests, and focal plane sweeps were completed. In this paper we present the data analysis process and compare the results from our models to measured X-ray centroid data, X-ray performance data, and out of focus images of the mirror pair.

Keywords: X-ray optics, X-ray telescopes, segmented mirrors, X-ray testing

1. INTRODUCTION

During the past several years the NGXO group at Goddard Space Flight Center (GSFC) have developed new X-ray telescope technologies for astronomical applications. Major components of these technologies are mirror fabrication processes based on monocrystalline silicon [1,2], telescope mechanical and structural development based on meta-shell approach [3,4], and assembly and alignment processes based on simple 4-point mirror mount concepts [5,6].

Major advancement in the mirror fabrication occurred recently when the mirrors were processed using commercially available ion-beam figuring (IBF) technology. The optical performance of silicon mirrors processed through the IBF-process is now below 1 arc-sec in the X-ray energy range. Meta-shell approach [7] is based on mirror segmentation into smaller components ranging from about 15 to 30 degrees. Thin mirror segments are easier to fabricate, assemble, and align in the gravity field than thin full-shell optic. Downside of this approach is that there are many more optical components to assemble and align. Meta-shell approach in conjunction with 4-point mount also provides very stiff structural components to build up the telescopes in laboratory environment.

The optical design of the NGXO demonstration mirror technology is based on Wolter type 1 telescope consisting of paraboloidal primary mirrors and hyperboloidal secondary mirrors. In the design multiple pairs of mirrors are nested inside each other. NGXO project has concentrated the development effort on 3 innermost mirror pairs of the telescope. In this paper we present X-ray testing results for the segments of innermost telescope measured at GSFC [8] and PANTER (X-ray test facility of the Max-Planck-Institut für extraterrestrische Physik in Neuried, Germany) [9] X-ray beamline facilities. We also present modeling and simulation results in our effort to better understand the X-ray test

Space Telescopes and Instrumentation 2018: Ultraviolet to Gamma Ray, edited by Jan-Willem A. den Herder, Shouleh Nikzad, Kazuhiro Nakazawa, Proc. of SPIE Vol. 10699, 1069952 · © 2018 SPIE
CCC code: 0277-786X/18/$18 · doi: 10.1117/12.2312243

data, characteristic of GSFC and PANTER beamlines, mirror surface characteristics, and assembly and alignment processes.

2. OPTICAL DESIGN AND SURFACE QUALITY OF MIRRORS

NGXO telescope is based on conventional Wolter type 1 design. Several primary and secondary mirror pairs are stacked inside each other. The assembled and tested mirror segments (serial numbers 312P1025 and 312S1020) of the SMD07 test unit are the innermost pair of the NGXO telescope.

2.1. Optical Design

Optical design of the NGXO telescope was selected to match our existing fabrication and testing hardware. The axial focal length of the nested telescope is 8.4 m. Radial height of the primary mirror and secondary mirror at their intersection is 156.186 mm. Mirror segments are axially 100 mm long and azimuthally 30 degrees wide. There is a 20 mm gap between the primary mirrors and secondary mirrors. The mirrors in the optical design are 0.5 mm thick.

2.2. Surface quality of mirrors

The 312P1025 primary mirror and 312S1020 secondary mirror were selected for the construction of SMD07 telescope. Mirror figure errors were measured in a 3-point mount using custom designed cylindrical null lens [10]. During the measurements, the mirrors were oriented so that their center azimuths were approximately parallel with the gravity vector. Figures 1 and 2 show the surface errors of the mirrors after the IBF-process of the primary mirror and secondary mirror, respectively. In top part of the Figures 1 and 2, axial radius variation, axial cone-angle variation, and axial sag variation are depicted. Root-Mean-Square (RMS) values of these quantities are shown in Table 1. All the errors are very small. Their contribution to the optical performance of the telescope is small. Lower part of the

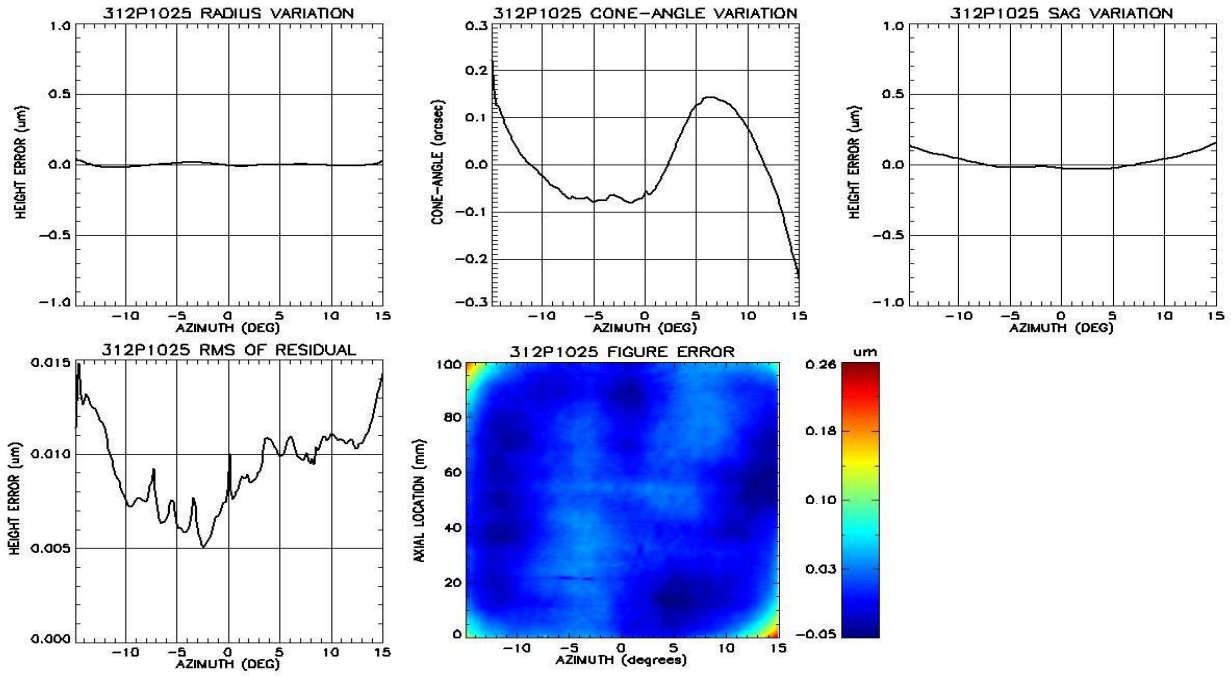

Figure 1. Measured surface errors of the primary mirror. Plots show the radius, cone-angle, sag, and residual height error variations. Contour plot show the overall figure error of the primary mirror.

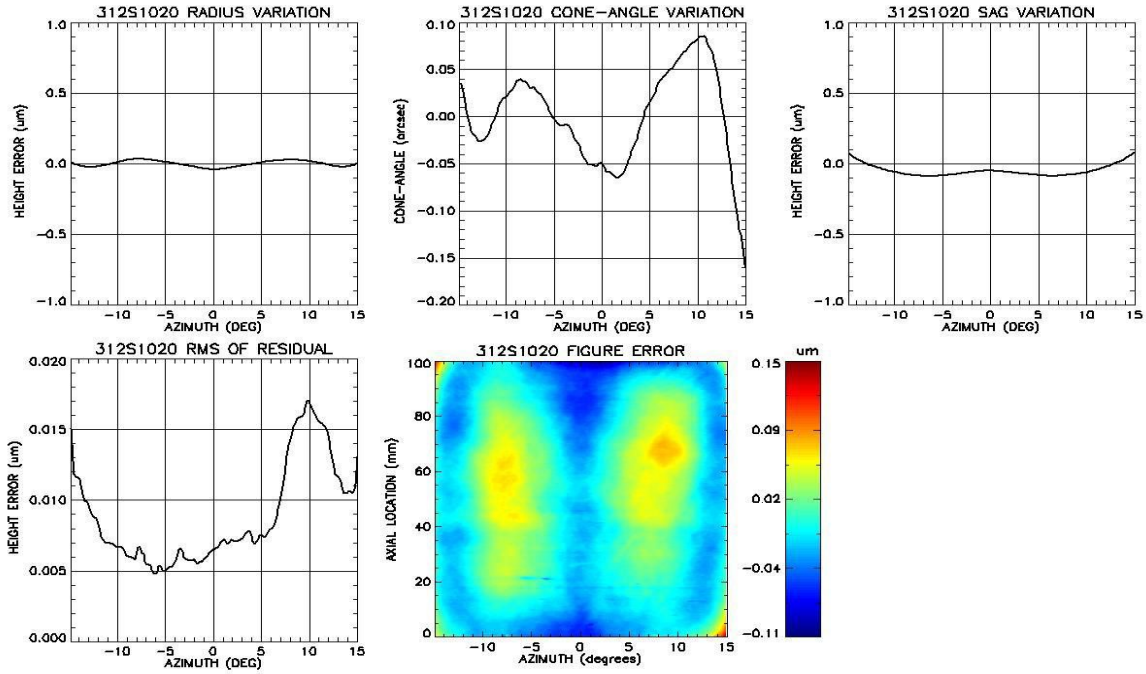

Figure 2. Measured surface errors of the secondary. Plots show the radius, cone-angle, sag, and residual height error variations. Contour plot show the overall figure error of the secondary mirror.

Table 1. RMS values of the surface errors calculated from surface metrology data and FEA data of the primary mirror and secondary mirror.

	Radius variation (μm)	Cone-angle variation (arc − sec)	Sag variation (μm)	Residual height error (μm)	Figure error (μm)
Primary mirror metrology	0.011	0.091	0.052	0.002	0.025
Secondary mirror metrology	0.021	0.050	0.042	0.004	0.031
Primary and secondary mirror (FEA)	0.004	0.0	0.006	0.004	0.038

Figures 1 and 2 plot the residual RMS axial figure errors and overall mirror figure errors. Lowest order radial height errors (average-radius errors) or cone-angle errors (delta-radius errors) of the mirrors were not measured.

2.3. FEA models of the mirrors

Detailed Finite Element Analysis (FEA) models of the mirrors were generated. The models included analyses of the mirrors mounted on the 4-point mount. The analysis simulated orientation of the mirrors in the assembly and alignment process in the 'frown' configuration (gravity vector parallel with the center radius of the mirror and the optical surface of the mirrors facing down). Also, detailed models of the epoxy curing processes between the posts and mirror surfaces were simulated.

Figure 3 shows the deformations of the secondary mirror in the gravity field after epoxy curing process is complete. Gravity and epoxy curing generates large peaks at the post locations. As expected, cone-angle and sag variations are extremely small. Radius variation is larger because the gravity is pulling down the sides of the mirrors and the mirrors are not as stiff in the azimuthal direction. Fortunately, its contribution to the image is very small, since radius variation generates azimuthal errors. Deformations of the primary mirror are nearly the same. RMS errors of the analyzed quantities are listed in Table 1.

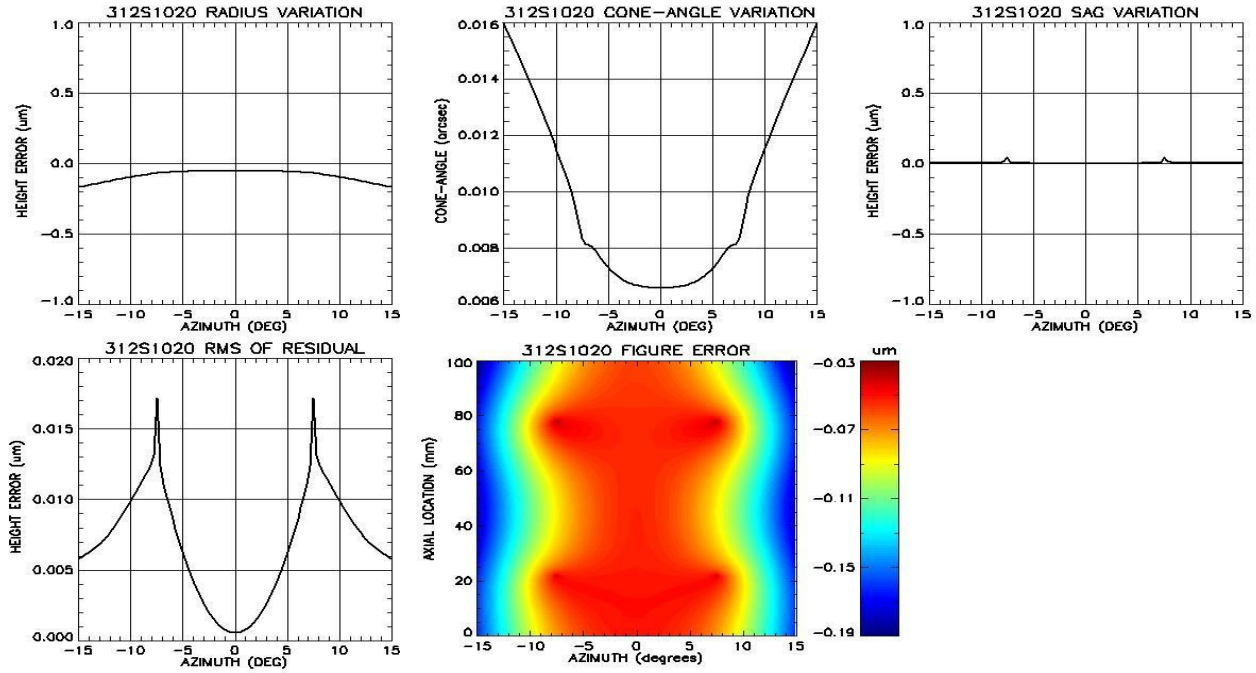

Figure 3. Radius, cone-angle, sag, and residual height error variations of the secondary mirror. Contour plot shows overall figure error of the mirror. Errors of the primary mirror are nearly identical.

3. ANALYSIS OF X-RAY DATA

SMD07 mirror module was tested first at GSFC in the 600-meter long X-ray beamline facility and later in PANTER 120-meter long beamline facility in Germany. The detector used in the GSFC measurements had 13 μm pixels size and the detector used in the PANTER facility had a 20 μm pixel size. SMD07 was tested using titanium source at the GSFC facility and carbon, copper, aluminum, and silver sources at the PANTER facility. Testing included measurements covering focus search and alignment processes of the mirror pair, full-aperture testing of the mirror pair and sub-aperture Hartmann scans of the full aperture. A series of intra- and extra-focal images were taken in ±250 mm focal plane range.

3.1. Analysis of full-aperture data

Figure 4 shows a set of full-aperture images measured at the GSFC facility. The detector was moved axially at 1-mm intervals through the focus in -4.0 mm to +1.0 mm range. Shapes of the images resemble a bowtie where the center of the bowtie moves up when the detector is scanned through the focus. Tails of the images focused by the azimuthal sides of the mirrors are clearly longer and there is an asymmetry in the tails. The center of the bowtie is just a few pixels wide. Half Power Diameters (HPD) of the images range from 2.9 arc-sec to 3.4 arc-sec.

Figure 5 depicts a series of images measured at the PANTER facility at varying energies ranging from Carbon-K, Copper-L, Aluminum-K, to Silver-L. HPDs of the images vary from 2.5 arc-sec, 2.8 arc-sec, 2.7 arc-sec, to 2.9 arc-sec, respectively. Carbon-K image does not have a bowtie shape and the center of images at other energies do not form as tight waste line as the GSFC images. This is likely caused by a factor of 4.5 shorter light source distance in the PANTER facility. For example, extended source of 1.0 mm in diameter in PANTER would increase the image

size by 1.7 arc-sec. The increase at the GSFC facility would be about 0.3 arc-sec. In the PANTER images, SMD07 mirror pair is partially imaging some features of the light source.

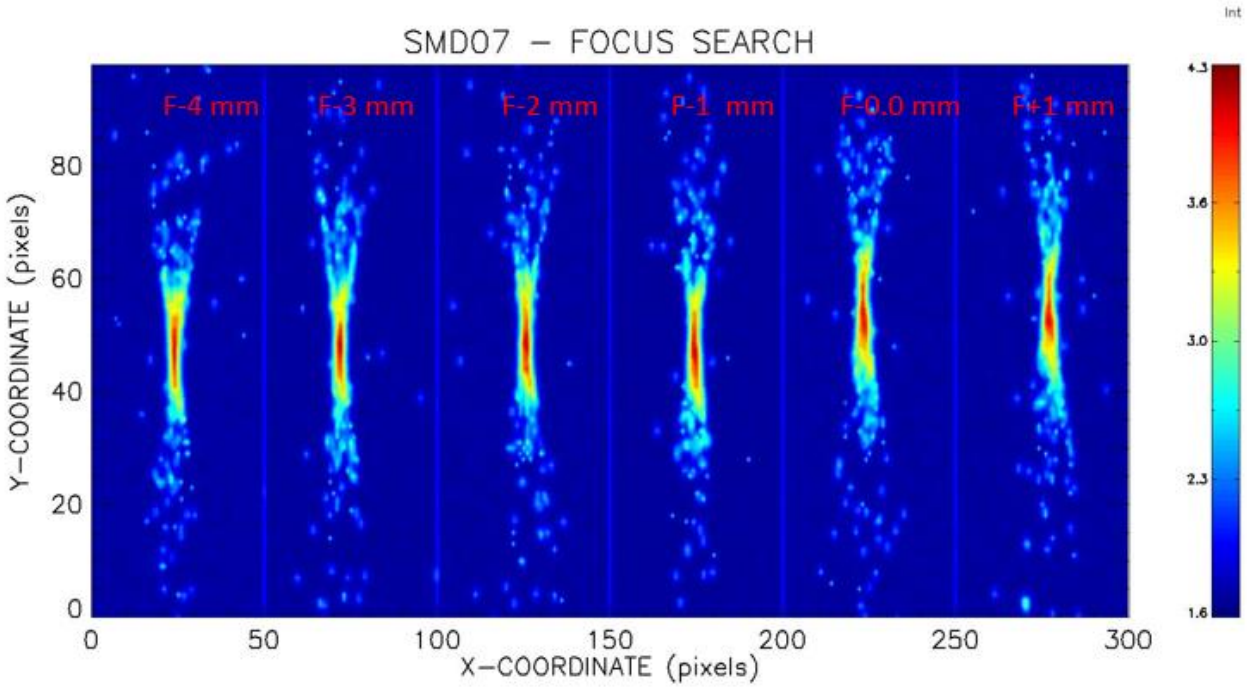

Figure 4. Images measured at GSFC using Ti-K light source. The detector was moved through the focus of the telescope. The best focus is located about 1 mm towards the telescope from nominal focus.

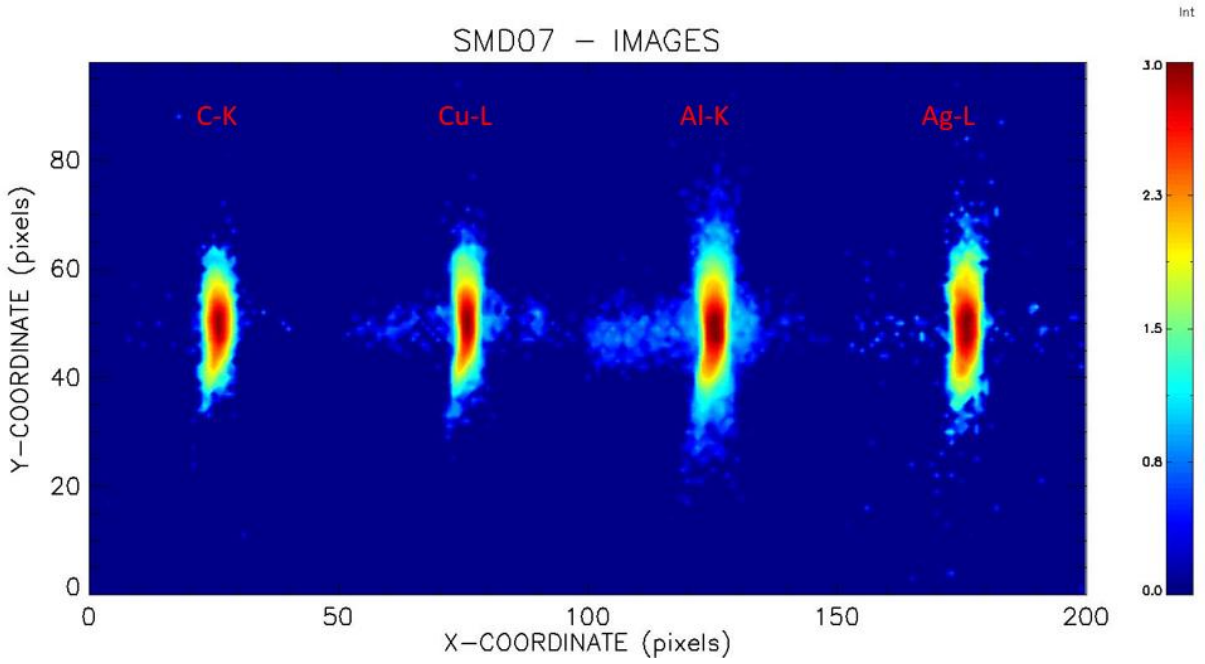

Figure 5. PANTER images measured at best focus locations at Carbon-K, Copper-L, Aluminum-K, and Silver-L energies.

3.2. Analysis of Hartmann data

During the Hartmann tests a 4-mm wide slit is moved across the front aperture of the SMD07 telescope. The detector was placed at the best focus of the telescope. Images were taken at 1.5-degree intervals. The Aluminum-K light source was used in the Hartmann tests. The centroids of the measured Hartmann images were calculated. The red curve in Figure 6 shows the centroid map calculated from the experimental data. The centroid curve consists of a simple loop and a long tail on one side of the image. Surface and alignment errors causing this type of simple image errors are a combination of pitch, yaw, decenter, average radius, and cone-angle errors of the mirrors. The detector can also be located slightly out of focus. Of these errors, pitch and decenter generate the coma aberration. Only partial loop of the double loops of coma is generated because the mirrors are 30-degree segments of full 360-degree circumference.

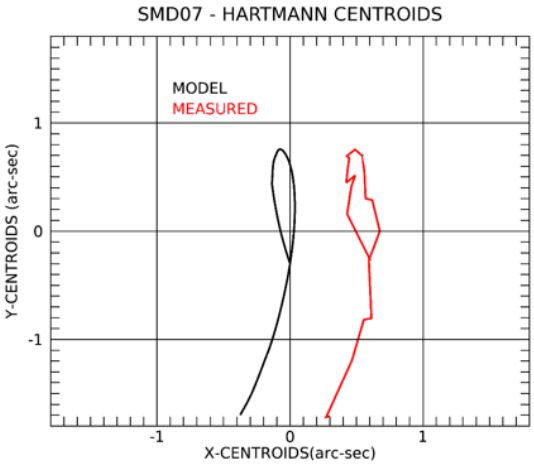

Figure 6. Centroid data calculated from measured data and alignment and surface errors of Table 2.

In the assembly process, potential cone-angle errors of the mirrors are compensated with equal amount of pitch error. This is done to minimize vignetting losses between the primary mirror and secondary mirror. Similarly, average radius errors are compensated with decentering of the mirror in order to catch most of the beam emanating from the other mirror. Combination of cone-angle and pitch errors generate image aberrations that are similar in shape as the errors generated by combination of average radius and decenter errors. These aberrations can be separated if the location of optical axis is known on the detector. However, average radius errors generate circumferential errors and they are significantly smaller than cone-angle errors. Ignoring the average radius and decenter errors the measured centroid data can be fit with parameters shown in Table 2.

Table 2. Values of cone-angle, pitch, yaw and defocus errors needed to fit the centroid data calculated from the Hartmann measurements.

	Cone-angle (arc-sec)	Pitch (arc-sec)	Yaw (arc-sec)	Defocus (mm)
Value	-27.2	27.2	1.9	2.0

The cone-angle and pitch errors are large. Cone-angle errors of the mirrors were not measured in the fabrication process or in the assembly and alignment process. The fitted error parameters are for the combination of the errors on the primary mirror and secondary mirror. The mirrors would have to be measured individually to determine the errors on individual mirror. A pair of segmented mirrors can tolerate large cone-angle errors because of the cone-angle-pitch compensation process. The black curve in Figure 6 shows the centroid curve calculated by ray tracing the SMD07 design with the error sources listed in Table 2. The resulting centroid curve matches well the centroid curve calculated from the experimental data.

The HPD variation of the SMD07 telescope was calculated from the Hartmann data by extracting line profiles from the Hartmann images and, then, calculating 1-dimensional HPDs. The black curve in Figure 7 plots the HPD as a function of the azimuth angle of the telescope calculated from the measured data. The 3-mm wide posts are located 7.2 degrees from the azimuthal edges of the mirrors. HPD tends to raise in and around these locations indicating small surface deformations caused by gravity and bonding. A larger increase in the HPD is seen on the right side in the Figure 7. A smaller increase is also caused by the posts on the right side deforming the mirrors. The red curve in Figure 7 shows the HPD variation calculated from mirror figure error metrology and FEA analysis of gravity and bonding deformations (model 1). The HPD variation of model 1 was calculated from the diffraction integral at 1.49 keV energy. There are still significant differences between the measured HPD variation and the HPD variation

calculated from the model 1 data. Assuming that the 4-point mounts of the mirrors generate mainly second order and fourth order axial errors, the measured HPD variation can be fit to a simple model consisting of the mirror surface figure errors, FEA models, assembly errors of Table 2, and additional axial second order sag and fourth order deformations. As illustrated in Figure 7, the HPD variation calculated from this set of errors (model 2) and placed on the primary mirror, matches the measured HPD variation well. Figure 8 shows the surface deformation caused by the assembly, alignment and bonding processes. The RMS value of the additional error is 0.076 µm. This deformation is the combined figure error of the primary and secondary mirrors. From the measured Hartmann data we do not know the distribution of the deformations on the primary mirror and on the secondary mirror.

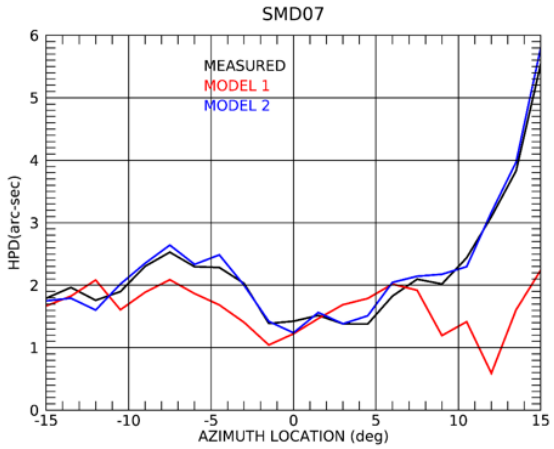

Figure 7. HPD variation calculated from measured X-ray data, model 1 data and model 2 data.

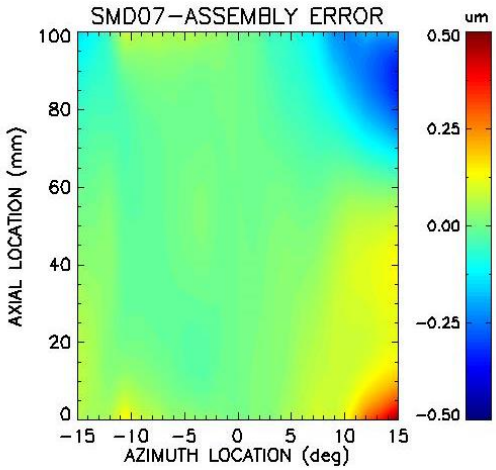

Figure 8. Telescope figure error contribution from assembly, alignment, and bonding processes. RMS error is 0.076 µm and peak-to-valley error is 0.86 µm.

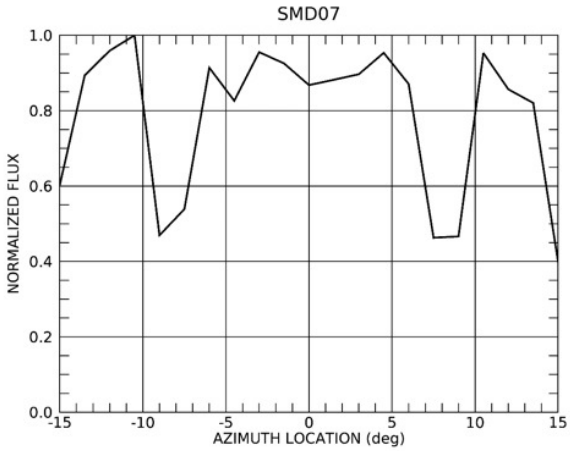

Figure 9. Flux of the SMD07 telescope calculated from the measured Hartmann data.

Figure 9 shows the normalized flux variation across the azimuth of the telescope. Flux was calculated from Hartmann images adding up all the pixels along the radial direction of the images and assuming 5 pixel azimuthal width of the images. The normalized flux is within ~10% across the azimuth expect on the side edges of the azimuth and at the obscured post locations.

3.3. SMD07 telescope X-ray performance

Table 3 compares the HPDs calculated from the experimental data measured at PANTER and GSFC. Also listed in Table 3 are the HPDs calculated from figure errors of model 1 and figure errors of model 2. GSFC and PANTER data were measured at 4.5 keV and 1.49 keV, respectively. The HPD of PANTER data calculated from the measured full-aperture image is 2.7 arc-sec. On the other hand, the HPD calculated from the surface errors of model 1 is 2.1 arc-sec. Figure 7 shows that the HPD variation of model 2 matches well with the HPD variation of the measured data. We conclude that the finite size of the light source increase the HPD from 2.1 arc-sec to 2.7 arc-sec. The HPD calculated from model 1 (included are the measured surface errors of the mirrors and FEA models of the mirrors) is 1.8 arc-sec. Assembly, alignment, and bonding deformations shown in Figure 8 increase the HPD from 1.8 arc-sec to 2.1 arc-sec.

HPDs calculated from the GSFC measured data and model 2 data at 4.5 keV are 2.9 arc-sec and 3.0 arc-sec, respectively. Longer light source distance (600 m) does not increase the HPD. At 4.5 keV the HPD decreases to 2.5 arc-sec if it is calculated from model 1 surface deformations.

Assembly, alignment, and bonding process clearly degrade the X-ray performance of 312P1025 and 312S1020 mirror pair. Optical performance of this mirror pair could be improved by additional ion beam figuring process. Key improvements should be the minimization on cone-angle errors, possible average radius errors, and low order axial errors.

Table 3. X-ray performance predictions of SMD07 mirror pair calculated from measured PANTER data, measured GSFC data, and surface deformation models1 and 2

	HPD (arc-sec)
HPD of full aperture image at 1.49 keV (Panter data)	2.7
HPD of model 2 at 1.49 keV	2.1
HPD of model 1 at 1.49 keV	1.8
HPD of full aperture image at 4.5 keV (GSFC data)	2.9
HPD of model 2 at 4.5 keV	3.0
HPD of model 1 at 4.5 keV	2.5

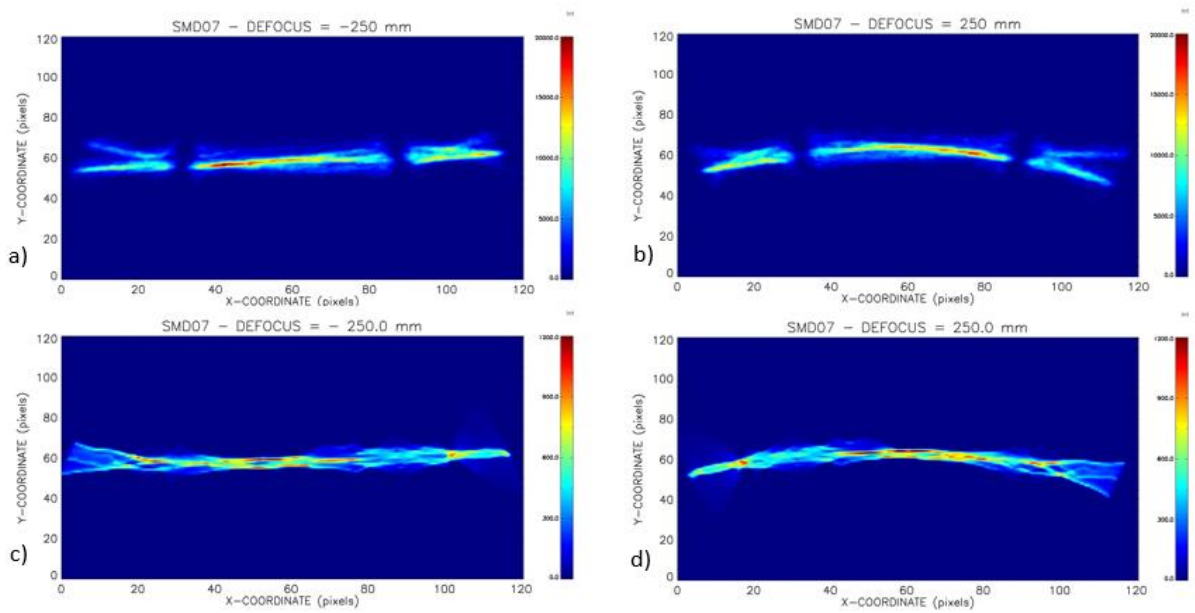

Figure 10. Plots a) and b) depicts intra-focal images measured ±250 mm from the focus of the SMD07 telescope. Plots c) and d) show simulated intra- and extra-focal images generated ±250 mm from the focus of the telescope.

3.4. Analysis of extra-focal and intra-focal data

Extra-focal and intra-focal images measured in the PANTER beamline facility reveal more information on the assembly/alignment errors and axial errors of the mirrors. Figures 10 a) and b) plot images measured -250 mm and +250 mm out of focus. As expected, images are horizontally reversed when the detector is moved from the intra-focal location to the extra-focal location. In the vertical direction, tilt and curvature changes of the images are not reversed. These changes can be related to cone-angle/pitch and yaw errors listed in Table 2. On the other hand, radial changes in the images are related to axial errors in the mirrors. Simulated images were generated by ray tracing the telescope. Measured metrology errors, FEA model errors, and model 2 deformations on the surfaces of the telescope were added

on the mirrors and the detector was placed ±250 mm out of focus. High frequency components of the measured metrology errors were filtered out to prevent radial smearing of the images. Figure 10 c) and d) show simulated images plotted from the ray trace results. These images exhibit the same features visible in the measured images of Figures 10 a) and b). On one side outside of the mounting posts, the images separate into two peaks. Added second order and fourth order axial errors cause the splitting of the radial images. Curing epoxy is mainly responsible for deforming the

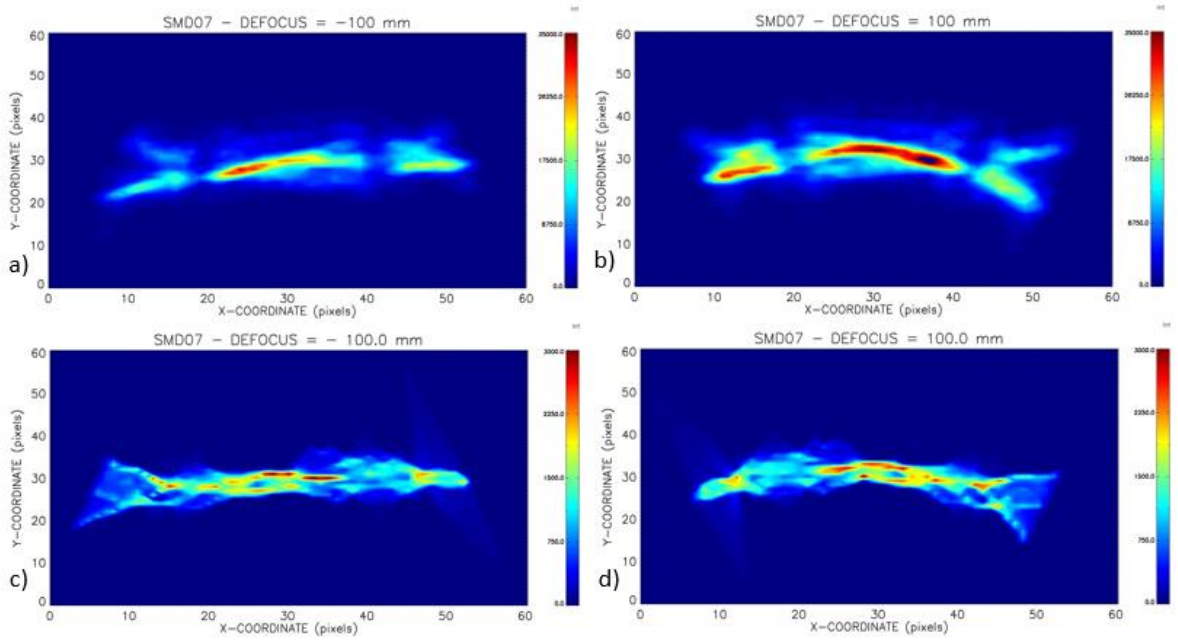

Figure 11. Images a) and b) were measured ±100 mm on both sides of the focus of the telescope. Images c) and d) show corresponding simulated images generated ±100 mm from the focus.

mirrors. Separation is much stronger on one side of the images. Slight separations are also seen on both sides of the mounting posts. These deformations are also caused the curing epoxy. Figures 11 a) and b) show the intra-focal and extra-focal images measured and at ±100 mm out of focus. Corresponding images generated from model 2 are shown in Figures 11 c) and d). Closer to the focus the shapes of the images change slightly but still have the same low order features.

4. Conclusions

X-ray tests performed at GSFC and PANTER X-ray beamlines show that the image quality of Wolter type 1 mirrors made out of monocrystalline silicon is in 2.1 arc-sec to 2.9 arc-sec range in the 0.3 keV-4.5 kev energy band. In general, measurements agree well. Characterization and understanding of the effects of light source on the image would further improve the agreement between the results.

Our fabrication process of the silicon based mirrors have significantly improved after ion bean figuring process was added to the fabrication cycle. Further improvements can be achieved by adding more ion beam figuring cycles to remove lowest order mirror axial and azimuthal errors.

The assembly process of the segmented mirrors is challenging. The process tends to generate surface deformations around and outside of the mounting points all the way to the outer azimuths of the mirrors. Mirrors are sensitive to the radial height errors of the mounting posts and gravity/epoxy curing effects during the assembly process. This can lead to localized errors that tend to be larger close to the azimuthal edges of the mirrors. Four mounting points of the mirrors typically generate cone-angle variation errors, possibly radius variation errors, axial second order sag errors,

and axial fourth order errors. Fortunately, pitch and yaw alignment adjustments during the assembly can be used to minimize the low order cone-angle errors.

5. ACKNOWLEDGEMENTS

The work leading to the results presented here has been financially supported by NASA through its ROSES/SAT and APRA programs and also in part by the European Union's Horizon 2020 Programme under AHEAD project (grant agreement no. 654215).

REFERENCES

[1] William Zhang, Kim Allgood, Michael Biskach, Kai-Wing Chan, Michal Hlinka, John Kearney, James Mazzarella, Ryan McClelland, Ai Numata, Lawrence Olsen, Raul Riveros, Timo Saha, and Peter Solly, "Monocrystalline silicon and the meta-shell approach to building X-ray astronomical optics, "Proc. of SPIE, **10399**, 103990S, (2017)

[2] William W. Zhang, "Next generation astronomical X-ray optics: high resolution, light weight, and low cost, "Proc. of SPIE, **10699**, these proceedings, (2018)

[3] Raul Riveros, Michael Biskach, Kim Allgood, John Kearney, Michal Hlinka, and William Zhang, "Progress on the fabrication of lightweight single-crystal silicon X-ray mirrors, "Proc. of SPIE. **10399**, 10399OT, (2017)

[4] Raul Riveros, Michael P. Biskach, Kim D. Allgood, John D. Kearney, Michal Hlinka, Ai Numata, and William W. Zhang, "Fabrication of lightweight silicon X-ray mirrors for high-resolution X-ray optics, "Proc. of SPIE **10699**, these proceedings (2018)

[5] Kai-Wing Chan, James Mazzarella, Timo Saha, William Zhang, Ryan McClelland, Michael Biskach, Raul Riveros, Kim Allgood, John Kearney, Marton Sharpe, Michal Hlinka, and Ai Numata, "Kinematic alignment and bonding of silicon mirrors for high-resolution astronomical X-ray optics, "Proc. of SPIE **10399**, 10399OU, (2017)

[6] Kai-Wing Chan, James R. Mazzarella, Timo T. Saha, Ryan S. McClelland, William W. Zhang, Peter M. Solly, Ai Numata, Raul E. Riveros, Michael P. Biskach, "Alignment and bonding of silicon mirrors for high-resolution X-ray optics, "Proc. of SPIE **10699**, (2018)

[7] Ryan McClelland, Joseph Bonafede, Timo Saha, Peter Solly, and William Zhang, "Design and analysis of an X-ray mirror assembly using the meta-shell approach, "Proc. of SPIE, **9905**, 99057A, (2016)

[8] https://asd.gsfc.nasa.gov/beamline/

[9] Vadim Burwitz, Richard Willingale, Carlo Pelliciari, Gisela Hartner, and Marlis-Madeleine La Caria, "Testing and calibrating the ATHENA optics at PANTER, "Proc. SPIE. **10399**, 103990O, (2017)

[10] David A. Content, David Colella, Theo Hadjimichael, John P. Lehan, Joseph McMann, Paul B. Reid, Timo T. Saha, and William W. Zhang, "Optical metrology for the segmented optics on the Constellation-X spectroscopy X-ray telescope, "Proc. of SPIE, **5488**, 272-282 (2004)